Draft version December 5, 2018
Typeset using LaTeX **twocolumn** style in AASTeX62

Predicting the Rossby number in convective experiments

Evan H. Anders,[1,2] Cathryn M. Manduca,[2] Benjamin P. Brown,[1,2] Jeffrey S. Oishi,[3] and Geoffrey M. Vasil[4]

[1] *Dept. Astrophysical & Planetary Sciences, University of Colorado – Boulder, Boulder, CO 80309, USA*
[2] *Laboratory for Atmospheric and Space Physics, Boulder, CO 80303, USA*
[3] *Department of Physics and Astronomy, Bates College, Lewiston, ME 04240, USA*
[4] *University of Sydney School of Mathematics and Statistics, Sydney, NSW 2006, Australia*

(Received October 19, 2018; Revised December 5, 2018; Accepted ??)

Submitted to ApJL

ABSTRACT

The Rossby number is a crucial parameter describing the degree of rotational constraint on the convective dynamics in stars and planets. However, it is not an input to computational models of convection but must be measured ex post facto. Here, we report the discovery of a new quantity, the Predictive Rossby number, which is both tightly correlated with the Rossby number and specified in terms of common inputs to numerical models. The Predictive Rossby number can be specified independent of Rayleigh number, allowing suites of numerical solutions to separate the degree of rotational constraint from the strength of the driving of convection. We examine the scaling of convective transport in terms of the Nusselt number and the degree of turbulence in terms of the Reynolds number of the flow. Finally, we describe the boundary layers as a function of increasing turbulence at constant Rossby number.

Keywords: convection — hydrodynamics — turbulence — dynamo — Sun: rotation

1. INTRODUCTION

Rotation influences the dynamics of convective flows in stellar and planetary atmospheres. Many studies on the fundamental nature of rotating convection in both laboratory and numerical settings have provided great insight into the properties of convection in both the rapidly rotating regime and the transition to the rotationally unconstrained regime (King et al. 2009; Zhong et al. 2009; Schmitz & Tilgner 2009; King et al. 2012; Julien et al. 2012; King et al. 2013; Ecke & Niemela 2014; Stellmach et al. 2014; Cheng et al. 2015; Gastine et al. 2016) The scaling behavior of heat transport, the nature of convective flow structures, and the importance of boundary layer-bulk interactions in driving dynamics are well known. Yet, we do not know of any simple procedure for predicting the magnitude of vortical flow gradients purely from experimental control parameters, such as bulk rotation rate and thermal input.

Corresponding author: Evan H. Anders
evan.anders@colorado.edu

In the astrophysical context, many studies of rotating convection have investigated questions inspired by the solar dynamo (Glatzmaier & Gilman 1982; Busse 2002; Brown et al. 2008, 2010, 2011; Augustson et al. 2012; Guerrero et al. 2013; Käpylä et al. 2014). Even when these simulations nominally rotate at the solar rate, they frequently produce distinctly different behaviors than the true Sun, such as anti-solar differential rotation profiles (Gastine et al. 2014). It seems that these differences occur because the simulations produce less rotationally constrained states than the Sun. The influence of rotation results from the local shear gradients, and these are not direct input parameters. Recent simulations predict significant rotational influence in the deep solar interior, which can drastically affect flows throughout the solar convection zone (Featherstone & Hindman 2016; Greer et al. 2016). In the planetary context, the balance between magnetic and rotational forces likely leads to the observed differences between ice giant and gas giant dynamos in our solar system (Soderlund et al. 2015). In particular, Aurnou & King (2017) suggest that many studies of planetary systems have over-emphasized the importance of magnetism compared to rotation.

In short, simulations must achieve the proper rotational balance if they are to explain the behavior of astrophysical objects. In Boussinesq studies, rotational constraint is often measured by comparing dynamical and thermal boundary layers or deviation in heat transport from the non-rotating state (King et al. 2012; Julien et al. 2012; King et al. 2013). Such measurements are not available for astrophysical objects, where the degree of rotational influence is best assessed by the ratio between nonlinear advection magnitude and the linear Coriolis accelerations. The *Rossby number* is the standard measure of this ratio,

$$\mathrm{Ro} \;\equiv\; \frac{|\nabla \times \boldsymbol{u}|}{2|\boldsymbol{\Omega}|} \;\sim\; \frac{|(\nabla \times \boldsymbol{u}) \times \boldsymbol{u}|}{|2\boldsymbol{\Omega} \times \boldsymbol{u}|}, \tag{1}$$

where $\boldsymbol{\Omega}$ denotes the bulk rotation vector. Many proxies for the dynamical Rossby number exist that are based solely on input parameters, most notably the *convective* Rossby number. However, all proxies produce imperfect predictions for the true dynamically relevant quantity.

> *In this letter, we demonstrate an emperical method of predicting the output Rossby number of convection in a simple stratified system.*

In Anders & Brown (2017) (hereafter AB17), we studied non-rotating compressible convection without magnetic fields in polytropic atmospheres. In this work, we extend AB17 to rotationally-influenced, f-plane atmospheres (e.g. Brummell et al. 1996, 1998; Calkins et al. 2015). We determine how the input parameters we studied previously, which controlled the Mach and Reynolds numbers of the evolved flows, couple with the Taylor number (Ta, Julien et al. 1996), which sets the magnitude of the rotational vector.

In section 2, we describe our experiment and paths through parameter space. In section 3, we present the results of our experiments and in section 4 we offer concluding remarks.

2. EXPERIMENT

We study fully compressible, stratified convection under precisely the same atmospheric model as in AB17, but here we have included rotation. We study polytropic atmospheres with $n_\rho = 3$ density scale heights and a superadiabatic excess of $\epsilon = 10^{-4}$ such that flows are at low Mach number. We study a domain in which the gravity, $\boldsymbol{g} = -g\hat{z}$, and rotational vector, $\boldsymbol{\Omega} = \Omega\hat{z}$, are antiparallel (as in e.g., Julien et al. 1996; Brummell et al. 1996).

We evolve the velocity ($\boldsymbol{u}$), temperature (T), and log density ($\ln\rho$) according to the Fully Compressible Navier-Stokes equations in the same form presented in AB17, with the addition of the Coriolis term, $2\boldsymbol{\Omega} \times \boldsymbol{u}$, to the left-hand side of the momentum equation. We impose impenetrable, stress-free, fixed-temperature boundary conditions at the top and bottom of the domain.

We set the kinematic viscosity (ν), thermal diffusivity (χ), and strength of rotation (Ω) at the top of the domain by choosing the Rayleigh number (Ra), Prandtl number (Pr), and Taylor number (Ta),

$$\mathrm{Ra} = \frac{g L_z^3 \Delta S / c_P}{\nu\chi}, \;\; \mathrm{Pr} = \frac{\nu}{\chi}, \;\; \mathrm{Ta} = \left(\frac{2\Omega L_z^2}{\nu}\right)^2, \tag{2}$$

where L_z is the depth of the domain as defined in AB17, $\Delta S \propto \epsilon n_\rho$ is the specific entropy difference between $z = 0$ and $z = L_z$, and the specific heat at constant pressure is $c_P = \gamma/(\gamma-1)$ and $\gamma = 5/3$. Throughout this work we set $\mathrm{Pr} = 1$. The Taylor number relates to the often-quoted Ekman number by the equality $\mathrm{Ek} \equiv \mathrm{Ta}^{-1/2}$.

The *convective* Rossby number has provided (e.g., Julien et al. 1996; Brummell et al. 1996) a common proxy (based on input parameters) for the degree of rotational constraint,

$$\mathrm{Ro_c} \;=\; \sqrt{\frac{\mathrm{Ra}}{\mathrm{Pr\,Ta}}} \;=\; \frac{1}{2\Omega}\sqrt{\frac{g\,\Delta S}{c_p L_z}}. \tag{3}$$

This parameter measures the importance of buoyancy relative to rotation without involving dissipation. In section 3, we empirically demonstrate that the true Rossby number defined in equation 1 depends nonlinearly on $\mathrm{Ro_c}$.

The wavenumber of convective onset increases such that, $k_{\mathrm{crit}} \propto \mathrm{Ta}^{1/6}$ (Chandrasekhar 1961; Calkins et al. 2015). We study horizontally-periodic, 3D Cartesian convective domains with extents of $x, y = [0, 4(2\pi/k_{\mathrm{crit}})]$ and $z = [0, L_z]$. At large values of Ta, these domains are tall and skinny, as in Stellmach et al. (2014). We evolve our simulations using the Dedalus[1] pseudospectral framework, and our numerical methods are identical to those presented in AB17.

The critical value of Ra at which convection onsets also depends on Ta (see the black line in figure 1a), roughly according to $\mathrm{Ra_{crit}} \sim \mathrm{Ta}^{2/3}$ (Chandrasekhar 1961; Calkins et al. 2015). We have confirmed these scalings of $\mathrm{Ra_{crit}}(\mathrm{Ta})$ and $k_{\mathrm{crit}}(\mathrm{Ta})$ in our atmospheres using a linear stability analysis. Even taking account of linear theory, the dependence of the evolved nonlinear

[1] http://dedalus-project.org/

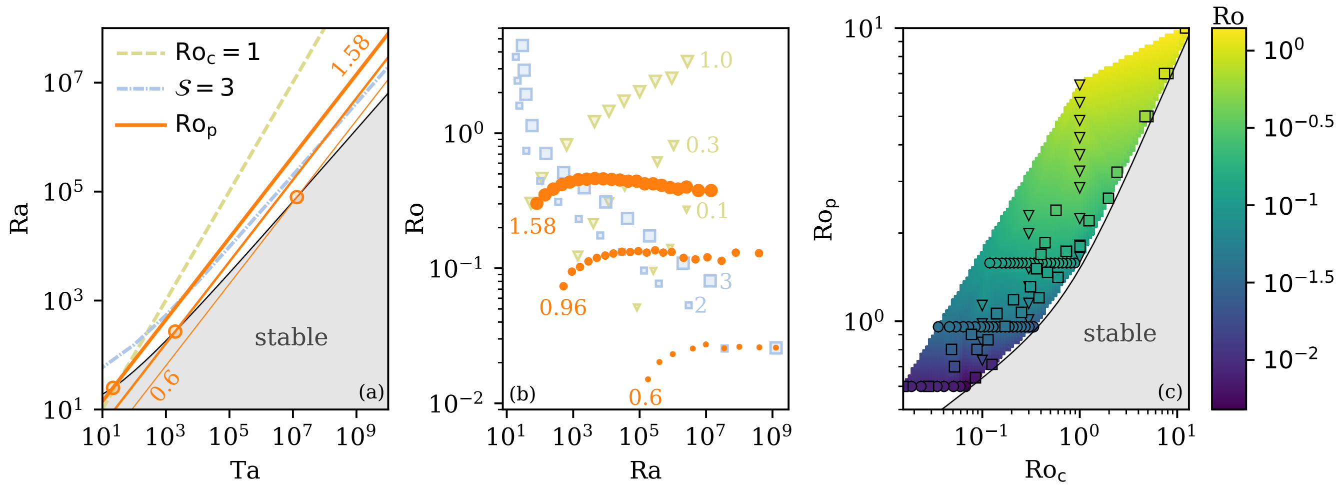

Figure 1. (a) The critical Rayleigh number, as a function of the Taylor number, is plotted as a solid black line. The grey shaded region is subcritical, and rotation supresses convection there. Paths of constant Convective Rossby number ($\mathrm{Ro_c}$, green dashed line), constant supercriticality ($\mathcal{S}$, blue dash-dot line), and constant Predictive Rossby number ($\mathrm{Ro_p}$, orange solid line) are shown. The three orange lines are plotted for $\mathrm{Ro_p} = [1.58, 0.96, 0.6]$ from thickest to thinnest, and the value of $(\mathrm{Ta_{crit}}, \mathrm{Ra_{crit}})$ for each line is denoted by a circular marker. (b) Evolved Ro is plotted vs. Ra along paths of $\mathrm{Ro_p}$= [1.58, 0.96, 0.6] for [big, medium, small] orange circles. For comparison, paths of constant $\mathcal{S}$ (blue squares, $\mathcal{S} = [3, 2]$ for [big, small] squares) and constant $\mathrm{Ro_c}$ (green triangles, $\mathrm{Ro_c}$ = [1, 0.3, 0.1] for [big, medium, small] triangles) are shown. Ro is roughly constant for a constant $\mathrm{Ro_p}$but changes drastically at constant $\mathrm{Ro_c}$ or $\mathcal{S}$. (c) The evolved value of Ro is shown as a function of $\mathrm{Ro_p}$ and $\mathrm{Ro_c}$. Each of the experiments in (b) is outlined by a black (circle, triangle, square) for points along constant ($\mathrm{Ro_p}$, $\mathrm{Ro_c}$, $\mathcal{S}$) paths. The color inside of the marker represents the exact measured Ro of that experiment, while the colormap outside of markers is a linear interpolation of the data set.

fluid flows on the input parameters makes predicting the rotational constraint very challenging. We will explore three paths through Ra-Ta space:

$$\mathrm{Ra} = \begin{cases} \mathcal{S}\,\mathrm{Ra_{crit}}(\mathrm{Ta}), & \text{(I)} \\ (\mathrm{Ro_c})^2\,\mathrm{Pr}\,\mathrm{Ta}, & \text{(II)} \\ (\mathrm{Ro_p})^2\,\mathrm{Pr}^{1/2}\,\mathrm{Ta}^{3/4} & \text{(III).} \end{cases} \tag{4}$$

Paths on constraint I are at constant supercriticality, $\mathcal{S} \equiv \mathrm{Ra}/\mathrm{Ra_{crit}}$ (blue dash-dot line in figure 1a). Paths on constraint II are at a constant value of the classic $\mathrm{Ro_c}$ (green dashed line in figure 1a). Paths on constraint III (e.g., orange solid line in figure 1a) set constant a ratio which we call the "Predictive Rossby number,"

$$\mathrm{Ro_p} = \sqrt{\frac{\mathrm{Ra}}{\mathrm{Pr}^{1/2}\,\mathrm{Ta}^{3/4}}} = \frac{1}{(2\Omega)^{3/4}}\sqrt{\frac{g\,\Delta S}{c_p\chi^{1/2}}} \tag{5}$$

Unlike paths through parameter space which hold $\mathrm{Ro_c}$ constant, paths with constant $\mathrm{Ro_p}$ feel changes in diffusivities but not the depth of the domain. To our knowledge, these paths have not been reported in the literature, although the importance of $\mathrm{Ra}/\mathrm{Ta}^{3/4} = \mathrm{Ra}\,\mathrm{Ek}^{3/2}$ has been independently found by King et al. (2012) using a boundary layer analysis. We compare our results to their theory in Section 4.

3. RESULTS

In our stratified domains, for sufficiently large $\mathrm{Ta} \geq 10^5$, a best-fit to results from a linear stability analysis provides $\mathrm{Ra_{crit}} = 1.459\mathrm{Ta}^{2/3}$ and $k_{\mathrm{crit}} = 0.414\mathrm{Ta}^{1/6}$. In figure 1a, the value of $\mathrm{Ra_{crit}}$ is shown as a function of Ta. A sample path for each criterion in equation 4 through this parameter space is shown. In figure 1b, we display the evolution of Ro with increasing Ra along various paths through parameter space. We find that Ro increases on constant $\mathrm{Ro_c}$ paths, decreases on constant $\mathcal{S}$ paths, and remains roughly constant along constant $\mathrm{Ro_p}$ paths. In figure 1c, the value of Ro is shown simultaneously as a function of $\mathrm{Ro_p}$ and $\mathrm{Ro_c}$ for all experiments conducted in this study. We find a general power-law of the form $\mathrm{Ro} = \mathcal{C}\mathrm{Ro_c}^{\alpha}\,\mathrm{Ro_p}^{\beta}$. In the rotationally-dominated regime where $\mathrm{Ro} < 0.2$ and $\mathrm{Re}_\perp > 5$ (see Eqn. 6), we find $\alpha = -0.02$, and Ro can be said to be a function of $\mathrm{Ro_p}$ alone. Under this assumption, we report a scaling of $\mathrm{Ro} = (0.148 \pm 0.003)\mathrm{Ro_p}^{3.34\pm0.07}$. In the less rotationally dominated regime of $\mathrm{Ro} > 0.2$ and $\mathrm{Re}_\perp > 5$, the scaling is less clear, and we find $\{C, \alpha, \beta\} = \{0.2, -0.19, 1.5\}$.

In figure 2, sample snapshots of the evolved entropy field in the x-y plane near the top of the domain are shown. In the left panel is a rotationally unconstrained flow at moderately high Ro, and Ro decreases into the

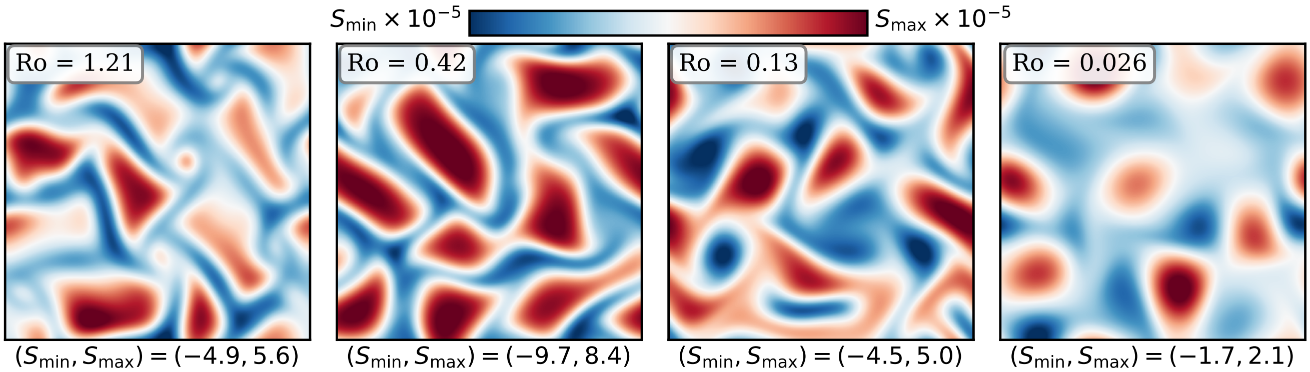

Figure 2. A horizontal slice of the evolved entropy field is plotted at $z = 0.95L_z$ for select simulations. The mean value of entropy at this height has been removed in all cases. All runs displayed here have an evolved volume-averaged $\mathrm{Re}_\perp \approx 32$. As Ro decreases from O(1) on the left to O(0.03) on the right, and thus the rotational constraint on the flow increases, significant changes in flow morphology are observed. At $\mathrm{Ro} = 1.21$ ($\mathrm{Ro_c} = 1$), convective dynamics are not hugely dissimilar from the non-rotating case where there are large upflows and narrow, fast downflow lanes (see e.g., AB17). As the rotational constraint increases, Coriolis forces more effectively deflect the convective flows, andthe granular convective pattern gives way to vortical columns.

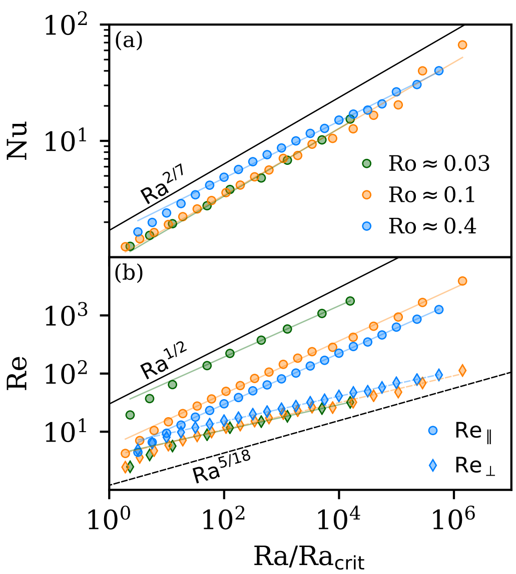

Figure 3. Scaling laws for paths at $\mathrm{Ro_p} = 1.58$ ($\mathrm{Ro} \approx 0.4$), $\mathrm{Ro_p} = 0.96$ ($\mathrm{Ro} \approx 0.1$), and $\mathrm{Ro_p} = 0.6$ ($\mathrm{Ro} \approx 0.3$) are shown. Numbers are plotted vs. $\mathrm{Ra}/\mathrm{Ra_{crit}}$, where $\mathrm{Ra_{crit}}$ is the value at which a given $\mathrm{Ro_p}$ path crosses the supercriticality curve (e.g., where the solid orange line crosses the black line in Fig. 1a). (a) The evolved scaling law of Nu approaches $\mathrm{Ra}^{1/3} \sim \mathrm{Ra}^{1/3}$, as expected from boundary layer theory (King et al. 2012). (b) $\mathrm{Re}_\parallel$ and $\mathrm{Re}_\perp$, as defined in equation 6, are shown. All values of $\mathrm{Ro_p}$ trace out similar $\mathrm{Re}_\perp$ tracks which scale roughly as $\mathrm{Ra}^{5/18}$, as expected. $\mathrm{Re}_\parallel$ tracks experience a constant offset for each different value of $\mathrm{Ro_p}$, but otherwise scale roughly as $\mathrm{Ra}^{1/2}$, as anticipated.

rotationally constrained regime from left to right. As Ro decreases, the classic granular structure of convection (see e.g., figure 2 in AB17) gives way to vortical columns of convection, as seen in rapidly rotating Rayleigh-Bénard convection (Stellmach et al. 2014). The select cases displayed in figure 2 each have an evolved volume-averaged $\mathrm{Re}_\perp \approx 32$ (defined below in equation 6).

We measure the Nusselt number (Nu), which quantifies heat transport in a convective solution, as defined in AB17. In figure 3a, we show how Nu scales as a function of Ra at fixed $\mathrm{Ro_p}$. We find that $\mathrm{Nu} \propto \{\mathrm{Ra}^{0.29\pm0.01}, \mathrm{Ra}^{0.29\pm0.01}, \mathrm{Ra}^{0.24}\}$ for $\mathrm{Ro_p} = \{0.6, 0.957, 1.58\}$. These scalings are in line with classic 2/7 power law scalings in Rayleigh-Bénard convection (Ahlers et al. 2009), and approach a $\mathrm{Ra}^{1/3}$ scaling, which has been predicted when $\mathrm{Ro_p}$ is held constant (see King et al. 2012, and section 4).

In our rotating domains, flows are distinctly different parallel to and perpendicular from the rotation vector, which aligns with gravity and stratification. We measure two forms of the RMS Reynolds number,

$$\mathrm{Re}_\parallel = \frac{|\boldsymbol{u}|L_z}{\nu}, \qquad \mathrm{Re}_\perp = \frac{|\boldsymbol{u}|}{\nu}\frac{2\pi}{k_{\rm crit}}, \tag{6}$$

where the length scale in $\mathrm{Re}_\perp$ is the wavelength of convective onset, and is related to the horizontal extent of our domain (see section 2). From our work in AB17, we expect the RMS velocity to scale as $|u| \propto \sqrt{\Delta S}$. By definition, $\nu \propto \sqrt{\mathrm{Ra}/(\mathrm{Pr}\ \Delta S)}$, and L_z is a constant set by the stratification while $k_{\rm crit} \propto \mathrm{Ta}^{1/6}$. Along paths of constant $\mathrm{Ro_p}$, we thus expect $\mathrm{Re}_\parallel \propto \mathrm{Ra}^{1/2}$ and $\mathrm{Re}_\perp \propto \mathrm{Ra}^{5/18}$ when Pr is held constant. In figure 3b, we plot $\mathrm{Re}_\parallel$ and $\mathrm{Re}_\perp$ as a function of $\mathrm{Ra}/\mathrm{Ra_{crit}}$ at fixed $\mathrm{Ro_p}$. We find that $\mathrm{Re}_\parallel \propto \{\mathrm{Ra}^{0.44\pm0.01}, \mathrm{Ra}^{0.45\pm0.01}, \mathrm{Ra}^{0.44}\}$ and $\mathrm{Re}_\perp \propto \{\mathrm{Ra}^{0.22\pm0.01}, \mathrm{Ra}^{0.23\pm0.01}, \mathrm{Ra}^{0.21}\}$ for $\mathrm{Ro_p} = \{0.6, 0.957, 1.58\}$. These scalings are similar to but

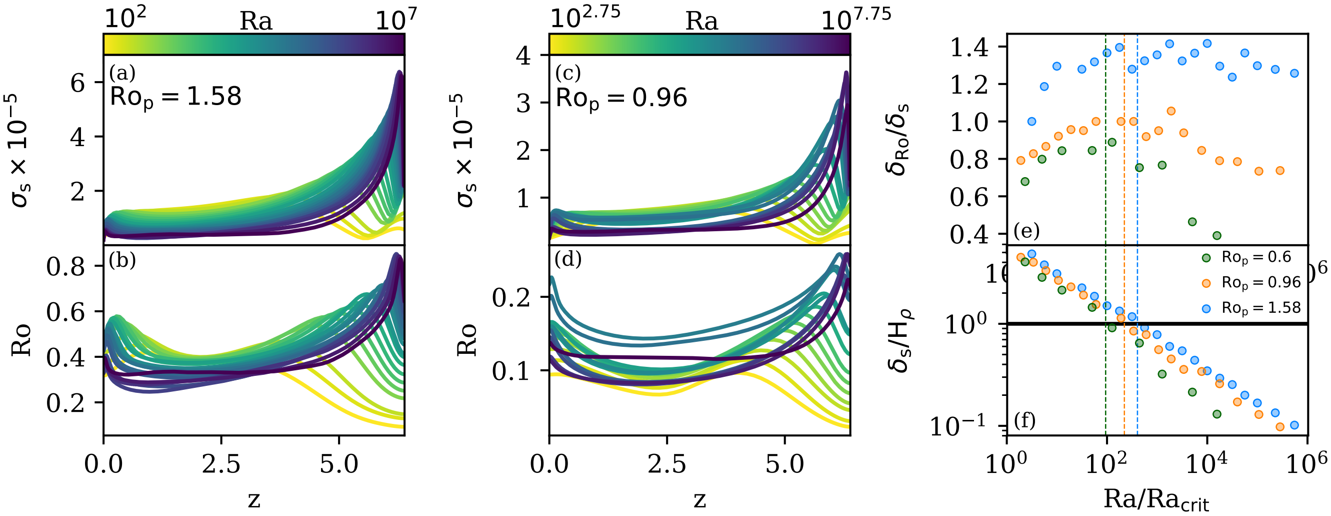

Figure 4. Horizontally-averaged profiles of the standard deviation of entropy(σ_s, a) and Rossby number (Ro, b) are shown vs. height for $\mathrm{Ro_p} = 1.58$ ($\mathrm{Ro} \approx 0.4$). Similar profiles are shown in (c) and (d) for $\mathrm{Ro_p} = 0.96$ ($\mathrm{Ro} \approx 0.1$). The color of the profiles denotes the value of Ra, with yellow profiles being at very low Ra and purple at the highest values of Ra studied here. (e) The ratio of the thicknesses of the dynamical (Ro) boundary layers and thermal (σ_s) boundary layers is shown for all values of $\mathrm{Ro_p}$ at each value of Ra. This ratio, and thus the relative importance of both thermal and rotational dynamics, seems to remain roughly constant across orders of magnitude of Ra. (f) We plot the size of the entropy boundary layer divided by the size of the density scale height at the top of the atmosphere. Vertical lines denote when these two length scales become equal, and we find that the size of the boundary layer compared to an important dynamical length scale does not predict any measurable change in system behavior.

slightly weaker than our predictions in all cases. Furthermore, $\mathrm{Re}_\perp$ collapses for each $\mathrm{Ro_p}$ track, while $\mathrm{Re}_\|$ experiences an offset to larger values as $\mathrm{Ro_p}$ shrinks. The offset in $\mathrm{Re_{parallel}}$ is unsurprising, because more rotationally constrained flows result in smaller boundary layers relative to the vertical extent of our stratified domain. The horizontal extent of our domain scales with the strength of rotation, and so regardless of the degree of rotational constraint, flows perpendicular to the rotational and buoyant direction are comparably turbulent at the same $\mathrm{Ra/Ra_{crit}}$. We find $\mathrm{Re}_\perp$ and $\mathrm{Re}_\|$ are respectively good proxies for the horizontal and perpendicular resolution required to run an experiment.

Figure 4 shows time- and horizontally-averaged profiles of Ro and the standard deviation of the entropy, σ_s. Figures 4a&b show these profiles for $\mathrm{Ro_p} = 1.58$ ($\mathrm{Ro} \approx 0.4$), while Figures 4c&d show these profiles for $\mathrm{Ro_p} = 0.96$ ($\mathrm{Ro} \approx 0.1$). The transition in profile behavior from low Ra (yellow) to high Ra (purple) is denoted by the color of the profile. As Ra increases at a constant value of $\mathrm{Ro_p}$, both the thermal (σ_s) and dynamical (Ro) boundary layers become thinner. We measure the thickness of the thermal boundary layer (δ_s) at the top of the domain by finding the location of the first maxima of σ_s away from the boundary. We measure the thickness of the Ro boundary layer (δ_Ro) in the same manner. In figure 4e, we plot $\delta_\mathrm{Ro}/\delta_s$, the ratio of the sizes of these two boundary layers. As anticipated, the dynamical boundary layer (δ_Ro) becomes relatively thinner with respect to the thermal boundary layer (δ_s) as Ro and $\mathrm{Ro_p}$ decrease. However, the precise scaling of this boundary layer ratio with $\mathrm{Ro_p}$ and Ra is unclear, and we cannot immediately compare these ratios to similar measures from the Rayleigh-Bénard convection literature, such as Fig. 5 of King et al. (2013). They measure the dynamical boundary layer thickness as the peak location of the horizontal velocities, but our horizontal velocities are subject to stress-free boundary conditions, and we find that the maxima of horizontal velocities occur precisely at the boundaries. In figure 4f, we plot δ_s in units of the density scale height at the top of the atmosphere, and we plot vertical lines when this crosses 1. We find no systematic change in behavior as a result of this stratification-based, important length scale.

4. DISCUSSION

In this letter, we studied low-Mach-number, stratified, compressible convection under the influence of rotation. We examined three paths through Ra-Ta space, and showed that the newly-defined Predictive Rossby number, $\mathrm{Ro_p} = \mathrm{Ra}/(\mathrm{Pr}^{\,1/2}\mathrm{Ta}^{3/4})$, determines the value of the evolved Ro.

In this work, we experimentally arrived at the $\mathrm{Ra/Ta^{3/4}} = \mathrm{Ra\,Ek^{3/2}}$ scaling in $\mathrm{Ro_p}$, but this relationship was independently discovered by King et al. (2012). Arguing that the thermal boundary layers should scale as $\delta_S \propto \mathrm{Ra}^{-1/3}$ and rotational Ekman boundary layers should scale as $\delta_{\mathrm{Ro}} \propto \mathrm{Ta}^{-1/4} = \mathrm{Ek}^{1/2}$, they expect these boundary layers to be equal in size when $\mathrm{Ra}/\mathrm{Ta}^{3/4} \sim 1$. They demonstrate that when $2 \lesssim \mathrm{Ra}/\mathrm{Ta}^{3/4} \lesssim 20$ flows are in the transitional regime, and for $\mathrm{Ra}/\mathrm{Ta}^{3/4} \lesssim 2$, flows are rotationally constrained. While our inclusion of stratification changes the precise values of Ra and Ta, the values of $\mathrm{Ro_p}$ studied here seem to fall in the rotationally constrained ($\mathrm{Ro_p} = 0.6$) or near-constrained transitional regime ($\mathrm{Ro_p} = \{0.957, 1.58\}$). The measured value of Ro (Fig. 1) and the observed dynamics (Fig. 2) seem to agree with this interpretation.

Despite the added complexity of stratification and despite our using stress-free rather than no-slip boundaries, the boundary layer scaling arguments put forth in King et al. (2012) seem to hold up in our systems. This is reminiscent of what we found in AB17, in which convection in stratified domains, regardless of Mach number, produced boundary-layer dominated scaling laws of Nu that were nearly identical to the scaling laws found in Boussinesq Rayleigh-Bénard convection.

We note briefly that the scaling $\mathrm{Ra} \propto \mathrm{Ta}^{3/4}$ is very similar to another theorized boundary between fully rotationally constrained convection and partially constrained convection predicted in Boussinesq theory, of $\mathrm{Ra} \propto \mathrm{Ta}^{4/5}$ (Julien et al. 2012; Gastine et al. 2016). This $\mathrm{Ta}^{4/5}$ scaling also arises through arguments of geostrophic balance in the boundary layers, and is a steeper scaling than the $\mathrm{Ta}^{3/4}$ scaling present in $\mathrm{Ro_p}$. This suggests that at sufficiently low $\mathrm{Ro_p}$, a suite of simulations across many orders of magnitude of Ra will not only have the same volume-averaged value of Ro (as in Fig. 1b), but will also maintain proper force balances within the boundary layers.

Our results suggest that by choosing the desired value of $\mathrm{Ro_p}$, experimenters can select the degree of rotational constraint present in their simulations. We find that $\mathrm{Ro} \propto \mathrm{Ro_p}^{3.34\pm0.07}$, which is within the 2σ of the estimate in King et al. (2013), who although defining Ro very differently from our vorticity-based definition here, find $\mathrm{Ro} \propto \mathrm{Ro_p}^{3.84\pm0.28}$. We note briefly that they claim that the value of Ro is strongly dependent upon the Prandtl number studied, and that low Ro can be achieved at high Pr without achieving a rotationally constrained flow. We studied only $\mathrm{Pr} = 1$ here, and leave it to future work to determine if the scaling of $\mathrm{Ro_p} \propto \mathrm{Pr}^{-1/4}$ is the correct scaling to predict the evolved Rossby number.

We close by noting that once $\mathrm{Ro_p}$ is chosen such that a convective system has the same Rossby number as an astrophysical object of choice, it is straightforward to increase the turbulent nature of simulations by increasing Ra, just as in the non-rotating case. Although all the results reported here are for a Cartesian geometry with antiparallel gravity and rotation, preliminary 3D spherical simulations suggest that $\mathrm{Ro_p}$ also specifies Ro in more complex geometries (Brown et al. 2019 in prep).

We thank Jon Aurnou and the anonymous referee who independently directed us to the work of King et al. (2012) during the review process, which greatly helped us understand the results of the experiments here. We further thank the anonymous referee for other helpful and clarifying suggestions. This work was supported by NASA Headquarters under the NASA Earth and Space Science Fellowship Program – Grant 80NSSC18K1199. EHA further acknowledges the University of Colorado's George Ellery Hale Graduate Student Fellowship. This work was additionally supported by NASA LWS grant number NNX16AC92G. Computations were conducted with support by the NASA High End Computing (HEC) Program through the NASA Advanced Supercomputing (NAS) Division at Ames Research Center on Pleiades with allocation GID s1647.

REFERENCES

Ahlers, G., Grossmann, S., & Lohse, D. 2009, Rev. Mod. Phys., 81, 503

Anders, E. H., & Brown, B. P. 2017, Physical Review Fluids, 2, 083501

Augustson, K. C., Brown, B. P., Brun, A. S., Miesch, M. S., & Toomre, J. 2012, ApJ, 756, 169

Aurnou, J. M., & King, E. M. 2017, Proceedings of the Royal Society of London Series A, 473, 20160731

Brown, B. P., Browning, M. K., Brun, A. S., Miesch, M. S., & Toomre, J. 2008, ApJ, 689, 1354

—. 2010, ApJ, 711, 424

Brown, B. P., Miesch, M. S., Browning, M. K., Brun, A. S., & Toomre, J. 2011, ApJ, 731, 69

Brummell, N. H., Hurlburt, N. E., & Toomre, J. 1996, ApJ, 473, 494

—. 1998, ApJ, 493, 955

Busse, F. H. 2002, Physics of Fluids, 14, 1301

Calkins, M. A., Julien, K., & Marti, P. 2015, Geophysical and Astrophysical Fluid Dynamics, 109, 422

Chandrasekhar, S. 1961, Hydrodynamic and hydromagnetic stability

Cheng, J. S., Stellmach, S., Ribeiro, A., et al. 2015, Geophysical Journal International, 201, 1

Ecke, R. E., & Niemela, J. J. 2014, PhRvL, 113, 114301

Featherstone, N. A., & Hindman, B. W. 2016, ApJ, 830, L15

Gastine, T., Wicht, J., & Aubert, J. 2016, Journal of Fluid Mechanics, 808, 690

Gastine, T., Yadav, R. K., Morin, J., Reiners, A., & Wicht, J. 2014, MNRAS, 438, L76

Glatzmaier, G. A., & Gilman, P. A. 1982, ApJ, 256, 316

Greer, B. J., Hindman, B. W., & Toomre, J. 2016, ApJ, 824, 4

Guerrero, G., Smolarkiewicz, P. K., Kosovichev, A. G., & Mansour, N. N. 2013, ApJ, 779, 176

Julien, K., Knobloch, E., Rubio, A. M., & Vasil, G. M. 2012, Physical Review Letters, 109, 254503

Julien, K., Legg, S., McWilliams, J., & Werne, J. 1996, Journal of Fluid Mechanics, 322, 243

Käpylä, P. J., Käpylä, M. J., & Brandenburg, A. 2014, A&A, 570, A43

King, E. M., Stellmach, S., & Aurnou, J. M. 2012, Journal of Fluid Mechanics, 691, 568

King, E. M., Stellmach, S., & Buffett, B. 2013, Journal of Fluid Mechanics, 717, 449

King, E. M., Stellmach, S., Noir, J., Hansen, U., & Aurnou, J. M. 2009, Nature, 457, 301

Schmitz, S., & Tilgner, A. 2009, PhRvE, 80, 015305

Soderlund, K. M., Sheyko, A., King, E. M., & Aurnou, J. M. 2015, Progress in Earth and Planetary Science, 2, 24

Stellmach, S., Lischper, M., Julien, K., et al. 2014, PhRvL, 113, 254501

Zhong, J.-Q., Stevens, R. J. A. M., Clercx, H. J. H., et al. 2009, Physical Review Letters, 102, 044502